Linear and Nonlinear Optical Field Manipulations with Multifunctional Chiral Coding Metasurfaces

Yifan Jiang, Wenwei Liu,* Zhancheng Li, Duk-Yong Choi, Yuebian Zhang, Hua Cheng,* Jianguo Tian, and Shuqi Chen*

Optical chirality, which describes the property of asymmetric light–matter interactions for different handedness of polarization, plays an important role in physical photonics, biochemical processes, and molecular recognition. Recently, asymmetric optical responses of chiral nanostructures provide a wide platform for arbitrary and artificial manipulation of optical chirality. Here, a design strategy is theoretically and experimentally introduced to realize a spin-selective coding metasurface in both linear and third harmonic regimes with giant chirality. Significant chiral transmission and wavefront control are realized by a chiral coding metasurface composed of amorphous silicon (a-Si) resonators with C_2 symmetry. The resonators and the enantiomers are encoded with different transmission amplitude and phase. The information channels are expanded to six-fold with simultaneous multi-foci focusing and multi-vortex generation operating in different polarization and linear/nonlinear channels. The nonlinear chiral high-contrast imaging is also achieved for spin-selective pattern information transmission. The study significantly expands the information capacity of coding metasurfaces, and can be readily applied in optical systems for information transmission in both linear and nonlinear regimes.

1. Introduction

Optical chirality, arising from the intrinsic asymmetry property of an optical system and its mirror image, is widely investigated in modern optics and photonics for applications such as biochemical processes and molecular recognition.[1–3] Generally,

Y. Jiang, W. Liu, Z. Li, Y. Zhang, H. Cheng, J. Tian, S. Chen
The Key Laboratory of Weak Light Nonlinear Photonics
Ministry of Education
Smart Sensing Interdisciplinary Science Center
Renewable Energy Conversion and Storage Center
School of Physics and TEDA Institute of Applied Physics
Nankai University
Tianjin 300071, China
E-mail: wliu@nankai.edu.cn; hcheng@nankai.edu.cn;
schen@nankai.edu.cn
D.-Y. Choi
Laser Physics Centre
Research School of Physics and Engineering
Australian National University
Canberra, ACT 2601, Australia
S. Chen
The Collaborative -Innovation Center of Extreme Optics
Shanxi University
Taiyuan, Shanxi 030006, China

the chiral light–matter interactions include two distinct phenomena: circular dichroism characterized by the absorption difference between transmitted left circularly polarized (LCP) and right circularly polarized (RCP) lights[4] and circular birefringence caused by phase accumulation difference between LCP and RCP lights.[5] Recently, chirality induced by artificial nanostructures and their 3D arrays-metamaterials has drawn much attention in the scientific community due to the arbitrary symmetric design and abundant optical resonance engineering of nanostructures. Such effects enable significant polarizability tensor manipulation of the optical fields with high degree of freedom (DOF).[6] Based on different local chiral electromagnetic resonances of the nanostructures, researchers have developed numerous functional chiral designs such as chiral biosensing,[7] chiral bound states in the continuum,[8] Janus plasmonic helical nanoapertures,[9] and weak chirality for strong coupling between resonant states.[10]

In the past decade, metasurfaces as planar counterparts of metamaterials have been extensively investigated due to their exotic electromagnetic properties for efficient scattering control of the electromagnetic waves.[11–15] In contrast to conventional optics, metasurfaces consist of arrays of subwavelength elements ("meta-atoms") that can locally manipulate light–matter interactions. Spatially varying meta-atoms allow the control of the polarization, phase, and amplitude of light, leading to high DOF to manipulate the electromagnetic waves from near-fields to far-fields.[16,17] The light–matter interactions supported by the meta-atoms include local multi-polar resonances[18,19] and near-field coupling resonances such as Fano resonances[20] and bound states in the continuum.[21,22] Generally, such resonances are accompanied by enhancement of local electric or magnetic fields, leading to enhanced nonlinear responses such as second harmonic generation (SHG) and third harmonic generation (THG).[23–25] Although the overall nonlinear efficiency of the reported metasurfaces is still not comparable to that in conventional nonlinear crystals, the nonlinear efficiency of metasurfaces is much higher when considering their planar nature. Most importantly, metasurfaces provide an efficient platform for optical frequency mixing and high harmonic generation.[26–28]

On the other hand, based on a variety of local resonances of meta-atoms, metasurfaces can be designed to carry different

**ADVANCED
SCIENCE NEWS**

www.advancedsciencenews.com

**ADVANCED
OPTICAL
MATERIALS**

www.advopticalmat.de

information channels when integrating different meta-atom arrays, such as multifunctional metasurfaces for multi-orbital angular momentum (OAM) generation[29] and coding metasurfaces for digital coding manipulation.[30–33] The building blocks of metasurfaces can be encoded with different informational wavefronts based on discontinuous phase abrupt. For example, Overvig et al. realized multifunctional nonlocal metasurfaces that can produce narrow band spatially tailored wavefronts at multiple selected wavelengths.[34] Wu et al. expanded the concept of coding metasurface to achieve nonlinear information transitions with spatiotemporal manipulation,[35,36] which remarkably improves the capacity and versatility of information processing based on meta-optics. However, to the best of our knowledge, the combination of chirality and digital coding elements in both linear and nonlinear regimes is still not realized, especially when carrying the information channels. This may potentially be applied in high-order information encryption and significantly enlarge the information capacity based on nonlinear photonics.

In this work, we theoretically and experimentally introduce a design strategy to realize a spin-selective coding metasurface in both linear and nonlinear regimes with giant chirality. The proposed metasurface consists of arrays of high refractive index amorphous silicon (a-Si) Z-shaped resonators belonging to the C_2 symmetry group, that breaks the in-plane mirror symmetry and induces cross-polarization conversion. Two linear and four THG optical channels with different focal lengths and topological charges can be simultaneously generated for various circularly polarized lights with different polarizations and wavelengths by introducing the coding patterns. The information capacity can be expanded to six-fold optical channels implementing the proposed scheme. The high-resolution chiral high-contrast imaging is also realized. Our approach significantly boosts the ability of multi-channel integrated optical communication and encoding information encryption on the subwavelength scale.

2. Results and Discussion

The schematic of the proposed design is shown in **Figure 1**a,b. The metasurface can generate different focusing channels and focused OAM channels with different topological charges for the cross-polarized fundamental frequency (FF) and THG signals with LCP and RCP incidences. The operating wavelengths, incident polarization states, and focal lengths are three designed DOF of the multifunctional metasurface, which are achieved by the chiral responses and spatial arrangement of the building blocks. The proposed metasurface consists of arrays of high refractive index a-Si Z-shaped resonators belonging to the C_2 symmetry group. It breaks the in-plane mirror symmetry and induces cross-polarization conversion in the linear optical regime. Meanwhile, based on the selection rule and nonlinear Pancharatnam–Berry (PB) phase in Ref. [37] the Z-shaped resonators also allow different phase dependence on the orientation angle of the resonator for different spin states of the THG signals. As a result, two linear and four THG optical channels with different focal lengths and topological charges can be simultaneously generated for various circularly polarized lights by introducing the coding patterns.
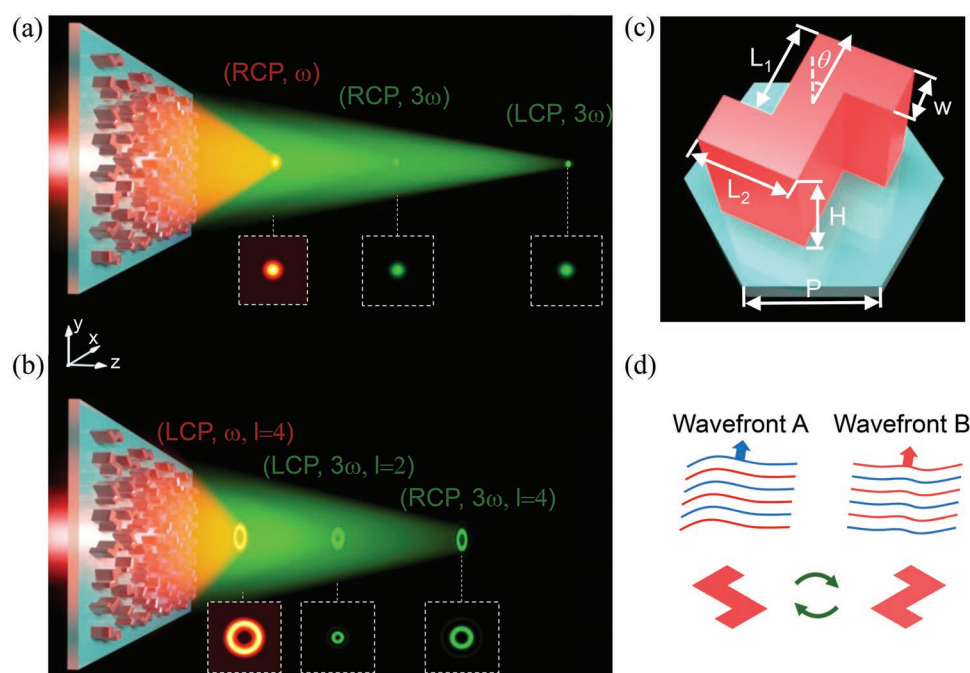

Figure 1. Schematic of the chiral functional metasurface with simultaneous linear and nonlinear generation. a) With LCP incidence, the chiral metasurface can simultaneously generate RCP-FF, RCP-THG, and LCP-THG focusing signals with different focal lengths. b) With RCP incidence, the chiral metasurface can generate LCP-FF, LCP-THG, and RCP-THG vortex beams with different topological charges and focal lengths. c) The building block of the a-Si metasurface on a fused silica substrate with a hexagonal lattice. The optimized structure has an arm length L_2 of 400 nm, a width w of 200 nm, a thickness H of 480 nm, and a cover layer with a thickness of 500 nm. d) The linear and nonlinear wavefront control is based on pairs of enantiomers.

2202186 (2 of 10)

To better characterize the chiral metasurface, we begin with the transmission matrix of the Z-shaped resonator, which possesses a mirror symmetry of M_{xy} (mirror symmetry with respect to the x-y plane) and a rotation symmetry of C_2 with respect to the z-axis. The transmission matrix of the metasurface can be written as $T = \begin{pmatrix} A & B \\ B & D \end{pmatrix}$, where $A = t_{xx}$, $B = t_{xy} = t_{yx}$ due to the structural rotational symmetry, and $D = t_{yy}$.[38] To further analyze the chiroptical responses, we change the Jones matrix from the Cartesian base to the circular base:

$$T_{circ} = \frac{1}{2} \begin{pmatrix} t_{xx} + t_{yy} & t_{xx} - t_{yy} - 2it_{xy} \\ t_{xx} - t_{yy} + 2it_{xy} & t_{xx} + t_{yy} \end{pmatrix} \quad (1)$$

To guarantee the chiral responses of the nanostructures, the mirror symmetries with respect to the x-z plane (M_{xz}) and y-z plane (M_{yz}) are broken to achieve the nonzero component of t_{xy}. We designed the all-dielectric Z-shaped resonator and its chiral enantiomer (Figure 1c,d) to realize the chiroptical responses originating from the excited electromagnetic modes. The hexagonal lattice is adopted to improve the duty cycle and eliminate the anisotropic electromagnetic resonances for various orientation angles θ of the nanostructure. More optimized details of the resonators can be found in the Experimental Section. The meta-atom on the substrate indeed breaks the mirror symmetry in the z-direction, resulting in $t_{xy} \neq t_{yx}$. This does not satisfy the hypothetical condition of the generalized anisotropic media. However, the effect is very week with the typically value $\Delta t / t_{xy}$ of $\approx 10^{-3}$, which can be neglected in the analysis model.

To examine the chirality of the proposed resonators working in circularly selective transmission mode, we simulated the modulo-squared transmission coefficients in the Jones matrix T_{LL}, T_{RL}, T_{LR}, and T_{RR} on circular basis (**Figure 2**a). The cross-polarization conversion rate from LCP to RCP can reach almost 1 at the resonance peak with the central wavelength of 1550 nm, which is much larger than the other three transmission coefficients. The measured circular polarization transmission spectra are consistent with the theoretical ones, indicating the significant chirality of the designed resonators (Figure 2b). The slight differences from the simulated spectra can be attributed to
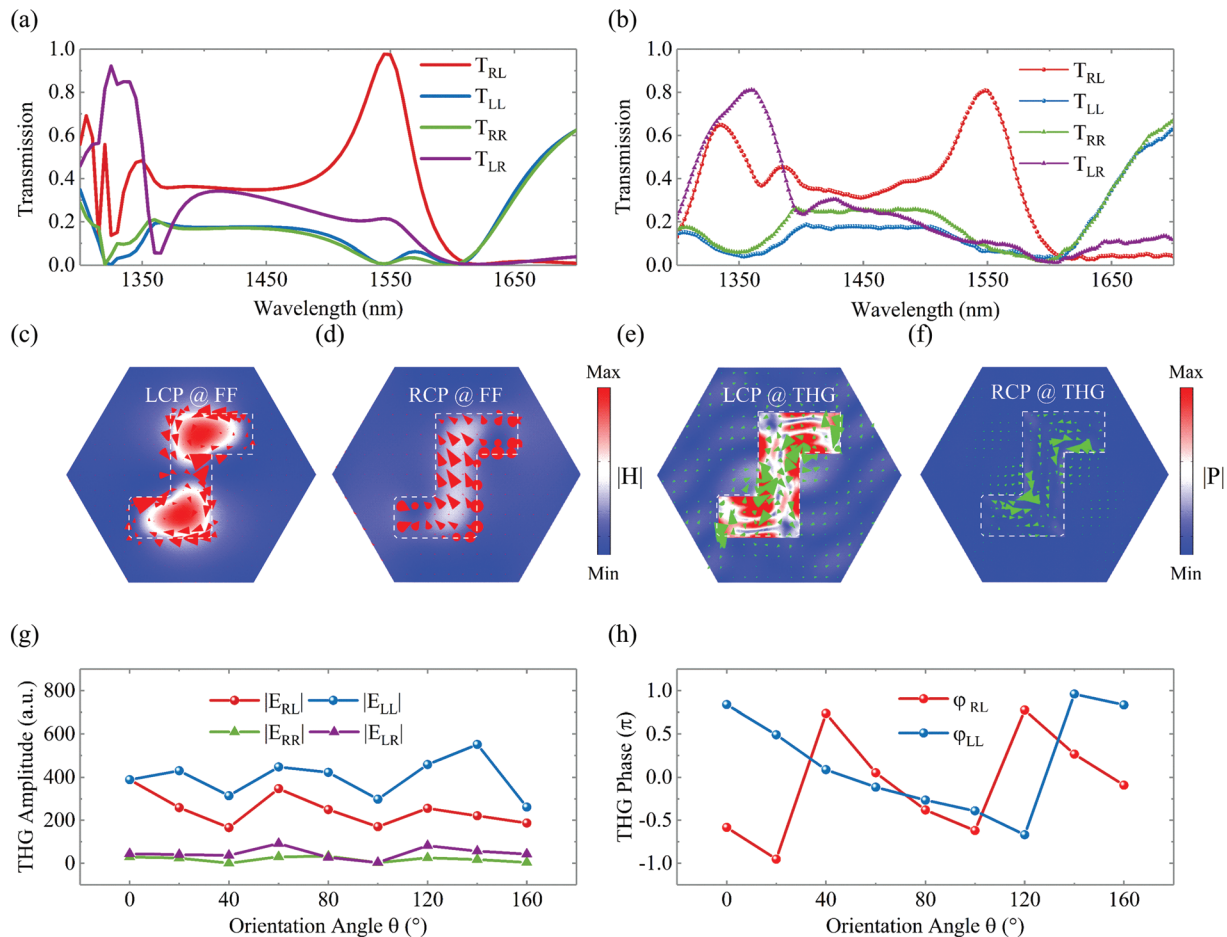

Figure 2. Simulated transmission and local resonances of the dielectric meta-atom. a) Simulated fundamental transmission spectra for circularly polarized incident lights of the periodically arranged chiral Z-shaped resonators. The resonance peak is around the wavelength of 1550 nm (the center wavelength of the femtosecond laser). b) Measured transmission spectra for circularly polarized incident lights of the resonators. c–f) Simulated (c,d) fundamental magnetic field distribution and e,f) nonlinear polarization intensity at the operating wavelength. The red and green arrows indicate the corresponding surface current distributions of fundamental and THG resonances. g,h) Simulated co-polarized and cross-polarized THG (g) amplitudes and (h) phase with LCP incidence as a function of orientation angles at the operating wavelength of 1550 nm.

the fabrication imperfections such as the rounded corners of the nanostructures, leading to the measured T_{LL} and T_{RR} with a magnitude of ≈0.07. The chiral transmission simulations based on the fabricated dimensions are well-consistent with the theoretical designs. The chiroptical responses result from the near-field chiral electromagnetic resonances of the nanostructures. The resonances can be in phase with constructive interference in one direction, while interactive destructively in the other direction. As a result, the breaking of degeneracy occurs between the circularly polarized lights of opposite handedness and the resultant chiroptical responses. The fundamental magnetic field distribution and THG polarization patterns are plotted for each circularly polarized incidence at the operating wavelength of 1550 nm in Figure 2c–f. For LCP incidence, there are two local magnetic field enhancement nodes with electric field vectors circulating around each resonator arm (Figure 2c), and strong THG polarization enhancement is observed inside the resonator (Figure 2e). In contrast, the magnetic near-fields are much weaker. We can hardly observe any field enhancement in the THG polarization pattern under RCP incidence (Figure 2d–f), suggesting that the resonance modes are circular-polarization selective in the chiral metasurface. Such chiroptical responses would exchange for the enantiomer of the resonator due to the mirror symmetry.

To manipulate the nonlinear wavefront of the chiral metasurface, the selection rule and nonlinear PB phase are considered in the design.[37] The harmonic generation is described by the relation $n = mj \pm 1$, where n is the harmonic order generated by the circularly polarized state σ ($\sigma = \pm 1$ implies LCP and RCP incident light respectively), j is an arbitrary integer, and m is the rotational symmetry of the nanostructures. Our resonators possess a twofold rotational symmetry. The wavefront manipulation of the fundamental and THG components can be obtained as quasi-independent channels. The PB phase of the generated signals is $(n \pm 1)\sigma\theta$ covering the complete phase space of 0–2π for different orientation angles θ (n takes 0 when considering the FF signals). As shown in Figure 2h, the phase of LCP-RCP signals is twice that of LCP-LCP signals, which can be employed to realize two different wavefronts of THG light. On the other hand, the calculated THG amplitudes of the two signal channels with LCP incidence stay in limited fluctuation for all orientation angles, while the THG amplitudes for RCP incidence are much smaller due to the chiral responses of the nanostructures (Figure 2g). The fluctuation of the THG amplitudes is caused by the weak interactions between adjacent resonators, which means a small portion of the electromagnetic energy locates outside of the nanostructures (Figure 2e), and such energy leak is affected by the orientation of the resonators. Although most of the dielectric meta-atoms operating at the fundamental frequency can be treated as independent between adjacent resonators, the leaky modes of nonlinear resonators can hardly be neglected as the wavelength is much shorter. The optical energy localizing inside the same resonator is more challenging, leading to quasi-guided modes in the metasurface, especially for oblique incidence.[39]

Allowed by these principles, we can design multifunctional coding metasurfaces carrying different information channels. As an example, an ultrathin flat metalens is designed with three modulated focal lengths in various channels (RCP-FF, RCP-THG, and LCP-THG), as shown in **Figure 3**a–c. Generally, a continuous hyperbolic phase distribution should be adopted $\phi_0(r) = k_0\sqrt{r^2 + f_0^2}$ for FF focusing, where k_0 is the linear wave vector, r is the distance of each meta-atom from the coordinate origin, and f_0 is the fundamental focal length. When the nth harmonic generation also realizes focusing, the phase function can be rewritten as $\phi_n(r) = k_n\sqrt{r^2 + f_n^2}$, where $\phi_n(r) = (n \pm 1)/2\phi_0(r)$, $k_n = nk_0$. However, this cannot be directly achieved because the phase of THG is locked up with the FF signals. We introduce the coding method to eliminate such binding. According to the Shannon's sampling theorem, the discrete sampling rate can vary the obtained Fourier components of signals. Starting from the focusing of the Fresnel zone plate composed of discrete phases, the optical path difference between two adjacent phase zones needs to satisfy:

$$\sqrt{r_{i+1}^2 + f^2} - \sqrt{r_i^2 + f^2} = \frac{\lambda}{N} \tag{2}$$

where r_i ($i = 1, 2, 3, ...$) is the outer radius of zone i and N represent the quantization order of the discrete phase distribution. In the paraxial approximation, Equation (2) can be rewritten as $r_{i+1}^2 - r_i^2 = 2\lambda f/N$. For the three channels, the wavelengths satisfy $3\lambda_{THG} = \lambda_{FF}$ and the phase quantization orders are governed by $N_{RCP-FF} = 2N_{RCP-THG} = N_{LCP-THG}$, and three-channel focusing is achieved by: $3f_{RCP-FF} = 2f_{RCP-THG} = f_{LCP-THG}$. We designed a binary-phase Fresnel zone plate for the RCP-THG channel with $r_1 = 8$ μm and $f_{RCP-THG} = 300$ μm. Based on the spatial phase distribution of the Fresnel zone plate and the relations between the three focusing channels, the phase pattern of the other two focusing channels can be achieved with $f_{RCP-FF} = 200$ μm and $f_{LCP-THG} = 600$ μm. The focusing optical vortices of different channels can be similarly designed by incorporating two distinct phase profiles of a lens and a vortex plate:

$$\varphi = \begin{cases} \frac{kr^2}{2f} + l \cdot \arctan\left(\frac{y}{x}\right), & x > 0 \\ \frac{kr^2}{2f} + l \cdot \left[\pi + \arctan\left(\frac{y}{x}\right)\right], & x < 0 \end{cases} \tag{3}$$

where the parameter l represents the topological charge of the radiated OAM light. We set the fundamental focal length $f_{RCP-FF} = 160$ μm with topological charge $l = 4$. Based on the aforementioned analysis, the two THG focusing optical vortices with $f_{RCP-THG} = 240$ μm, $l = 2$ and $f_{LCP-THG} = 480$ μm, $l = 4$ can be generated simultaneously in the same metasurface as shown in Figure 3d–f. The relation between the focal lengths of the three channels can be further applied in multi-channel imaging and information transmission. For example, by controlling the detection polarization, isometric imaging and Fourier transform can be simultaneously realized at the same imaging plane according to $2f_{RCP-THG} = f_{LCP-THG}$, which provides a possibility for single-shot and simultaneous information processing of nonlinear signals.

We characterize the specific performance of the designed metasurfaces in selecting certain channels by using the experimental setup, schematically shown in **Figure 4**a. The metasurface was fabricated through standard electron-beam lithography (EBL) procedure (see details in Experimental Section). Figure 4b
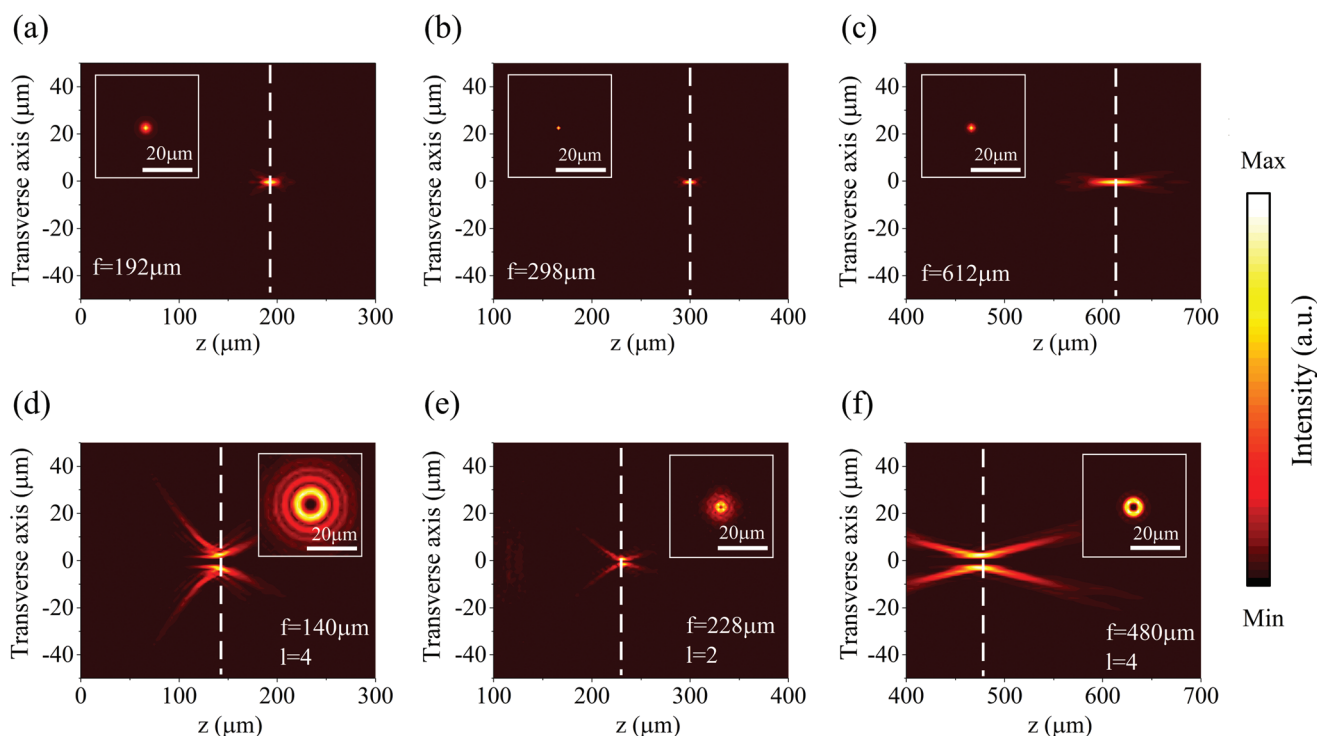
Figure 3. Calculated intensity profiles of the multifunctional focusing and vortex beam generation of the metasurfaces. a–c) Intensity distributions of the spin-selective metalens with modulated focal lengths for LCP incidence. The polarization and the corresponding functions of the metasurface are a) RCP-FF, b) RCP-THG, and c) LCP-THG, respectively. The insets show the intensity distributions at focal planes. d–f) Intensity distributions of the spin-selective metasurface with focusing optical vortex generation for LCP incidence. The polarization and the corresponding functions of the metasurface are d) RCP-FF with a charge of $l = 4$, e) RCP-THG with a charge of $l = 2$, and f) LCP-THG with a charge of $l = 4$, respectively. The insets show the intensity distributions at focal planes.

shows the scanning electron microscopy (SEM) images of the fabricated optical-vortices metasurface, in which the different colors of resonators represent distinctive orientation angles of meta-atoms. For an LCP fundamental incidence, the intensity distribution of three channels RCP-FF, RCP-THG, and LCP-THG were experimentally measured as shown in Figure 4c–e, which are inconsistent with the calculated ones. The measurement demonstrates that the spin-selective coding metasurface provides simultaneous focusing of linear and nonlinear components with various focal lengths in different channels. The measured focal lengths for different channels are $f_{RCP-FF} = 194$ µm, $f_{RCP-THG} = 296$ µm, and $f_{LCP-THG} = 524$ µm. Such enlarged focal lengths (compared with the ones set in Equation (2)) are caused by the parabolic phase distribution in the metasurface design, and the focal lengths match well with the calculated ones (Figure 3a–c). The measured full width at half-maximum (FWHM) values of the intensity distributions at the focal plane are 2.79, 3.24, and 4.19 µm respectively. The focusing optical vortices were also measured and the three channels intensity distributions are shown in Figure 4f–h. The diameter of the RCP-THG nonlinear annular ring is ≈13 µm which is smaller than the opposite polarization channel due to the smaller topological charge. This phenomenon can also be observed through the calculated intensity distributions.

Multifunctional chiral coding metasurfaces can be further realized by incorporating enantiomeric pairs of the resonators. Based on the mirror symmetry paired enantiomers exhibit giant

chiroptical responses and opposite spin-selective properties in the near-field enhancement. Therefore, with various circularly polarized incidences, the specific enantiomers in the same sample can be excited for either multifocal metalens or multi-vortex beam generation. The two completely different phase profiles are encoded in the same metasurface within opposite circularly polarized channels, as shown in **Figure 5**a–c. Specifically, with a fundamental incidence of LCP operating at 1550 nm, the transmitted RCP components of the FF and THG signal focus at 200 and 300 µm away from the sample plane, and the transmitted LCP component of THG signal is focused at 600 µm. The LCP component of the FF signal is eliminated due to the chiral response of the nanostructures. In contrast, when the helicity of the incident FF waves is inverted (RCP), distinct focusing optical vortices are generated in three channels simultaneously, that is a linear vortex with focal length $f_{LCP-FF} = 160$ µm and topological charge $l = 4$, two circularly polarized THG signal with $f_{LCP-THG} = 240$ µm, $l = 2$ and $f_{RCP-THG} = 480$ µm, $l = 4$ respectively. The functions of the metasurface are experimentally demonstrated in Figure 5d–i. Similar to the experimental results of the metalens sample (Figure 4d), there is also an intensity peak at $z = 205.5$ µm in the RCP-THG channel caused by the high-order diffraction, which enlarges the depth of focusing. For RCP incidence, the enantiomers in the designed phase arrangement function as optical vortices generators. Some background components in the RCP-THG channel are induced, leading to interference with the focusing
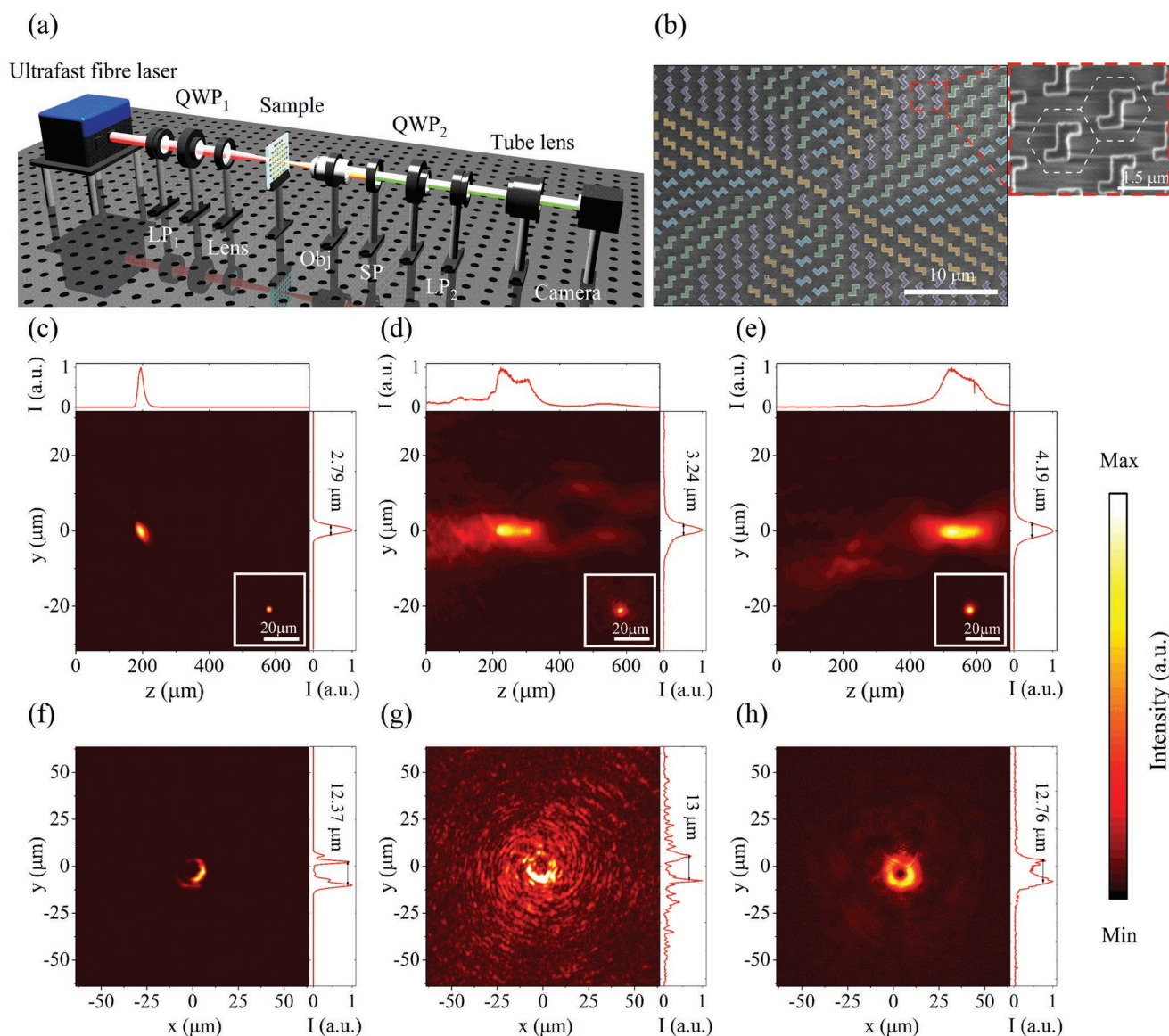
**ADVANCED
SCIENCE NEWS**

www.advancedsciencenews.com

**ADVANCED
OPTICAL
MATERIALS**

www.advopticalmat.de

Figure 4. Experimental demonstration of the chiral multifunctional metasurface with spin-selective focusing and vortex beam generation. a) Illustration of the experimental setup to measure the linear and nonlinear signals. LP, linear polarizer; QWP, quarter-wave plate; SP, short-pass filter. b) SEM images of the fabricated metasurface. c–e) Measured intensity distributions of the metalens in the y-z plane for different functions with c) RCP-FF, d) RCP-THG, and e) LCP-THG. The insets show the intensity distributions at the focal planes. f–h) Measured intensity distributions of the focusing optical vortices with f) RCP-FF, g) RCP-THG, and h) LCP-THG at focal planes.

vortex to generate a twisting pattern (Figure 5i). The topological charge can be obtained experimentally from the twisting pattern by counting the petals number of the encircling beam, that is $l = 4$. To better summarize the information channels of this approach, a comparison between the proposed multifunctional chiral metasurface and previous works is provided in **Table 1**. Compared with these previous works, our design expands the information capacity to six-fold optical channels in linear and nonlinear regimes.

Our scheme can also be readily applied in nonlinear chiral high-contrast imaging. Benefiting from the chiral-selective transmission of the pairs of enantiomers, the metasurface can be encoded with high-contrast images. As shown in **Figure 6a**, we designed a flower pattern with centrosymmetric, and the

black/white areas correspond to two kinds of enantiomers. The high-contrast third harmonic optical imaging enabled by the chiral resonances is expected. As shown in Figure 6b,c, the experimental images show a clear view of the pattern, with the exact configuration of five petals of each flower, two leaves, and a branch as the design target. The two flower images are complementary due to the complementary transmission coefficients of the enantiomers under opposite circularly polarized illumination. The information missing from the images is caused by two reasons. The intensity of incident the Gaussian beam decreases abruptly when the field of view is large. Thus, the marginal area of the image can hardly be distinguished. On the other hand, the meta-atoms are not perfectly shaped and the surfaces of the antennas are not completely smooth, resulting
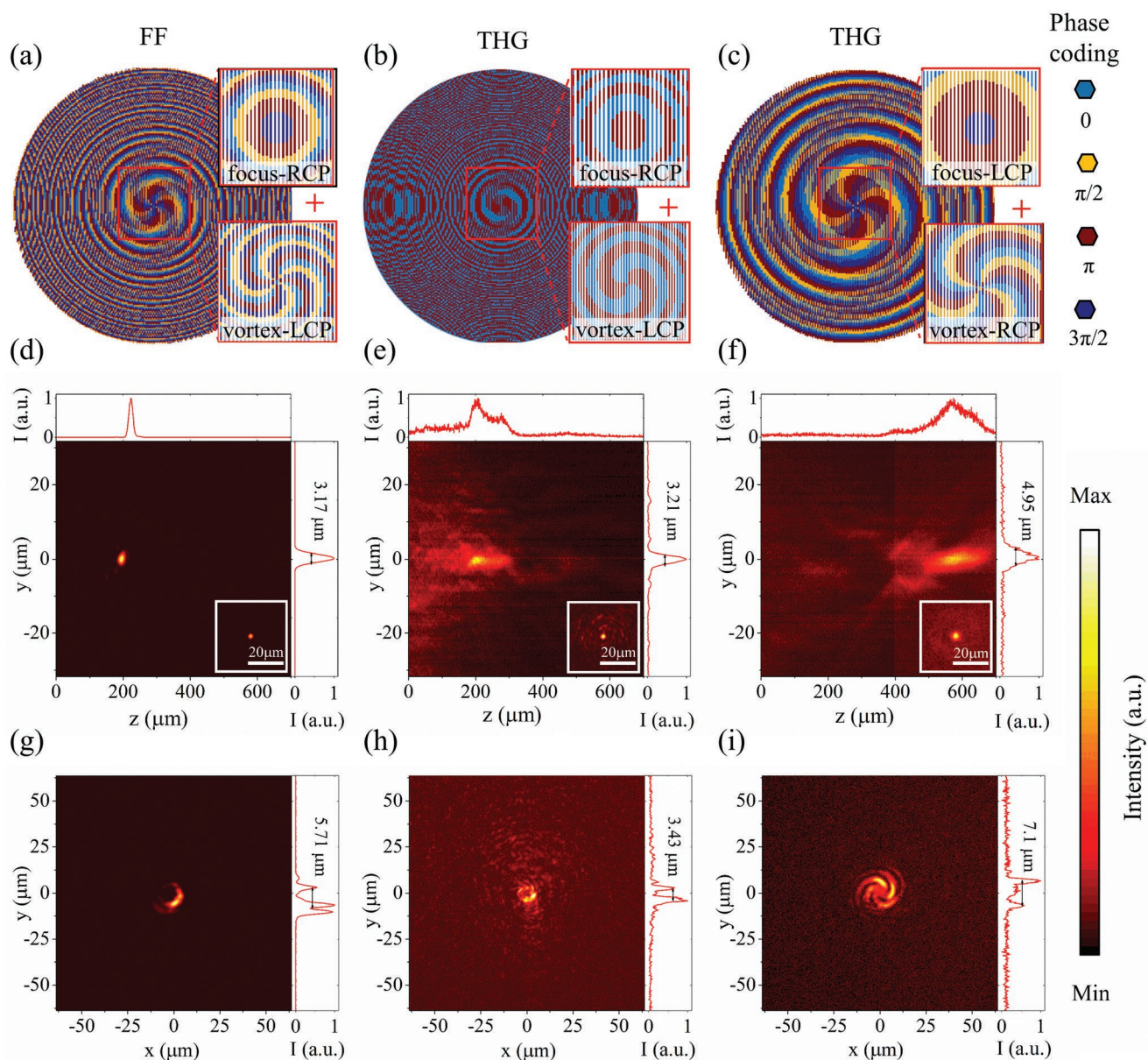
Figure 5. Measured chiral multifunctional metasurface with paired enantiomers. a–c) Phase designs for three different signal channels, in which the LCP and RCP functions are encoded. d–f) Measured intensity distributions of the chiral multifunctional metasurface for LCP incidence with d) RCP-FF, e) RCP-THG, and f) LCP-THG in the y-z plane. The insets show the intensity distributions at focal planes. g–i) Measured intensity distributions of the same sample works as focusing optical vortices with RCP incident for g) LCP-FF, h) LCP-THG, and i) RCP-THG at focal planes. The insets show the intensity distributions at focal planes along the y-axis.

in undesired scattering effects which can lower the overall nonlinear efficiency of the patterned metasurface. Our observation successfully proved the chiral selective transmission capability of the nonlinear metasurface, indicating that the enantiomers can effectively impart inverse patterns into opposite circularly polarized channels of THG waves.

3. Conclusion

In conclusion, benefitting from the unique chiral properties of the a-Si nanostructure with a twofold rotational symmetric geometry that induces cross-polarization conversion, we proposed a multifunctional chiral coding metasurface design that exhibits giant transmission asymmetry for different helicity of incident polarization. By introducing the PB phase and the chiral local electromagnetic resonances, the transmitted cross-polarized FF and both spin-states THG signals are encoded with different wavefronts, which expand the information capacity to six-fold optical channels in the linear and nonlinear regimes. The strict quantitative relation between different channels may also benefit simultaneous imaging and information processing for different polarization states. Featured with these extraordinary properties, we theoretically designed and experimentally

**ADVANCED
SCIENCE NEWS**

www.advancedsciencenews.com

**ADVANCED
OPTICAL
MATERIALS**

www.advopticalmat.de

Table 1. Comparison with other chiral metasurfaces.

Ref.	Material	Linear/nonlinear	Phase	Function	Channel num.
[40]	Dielectric	Linear	PB	Splitter	2
[41]	Plasmonic	Nonlinear	Resonance	Vortex	2
[42]	Dielectric	Nonlinear	Propagation	Metalens	1
[43]	Dielectric+plasmonic	Nonlinear	PB	Holography	2
[44]	Dielectric	Linear	PB + propagation	Imaging	2
This work	Dielectric	Linear + nonlinear	PB	Metalens + vortex + imaging	6

demonstrated the multi-foci metalens and multi-vortex beam generation with various focal lengths and topological charges in each channel. Furthermore, to confirm the circular polarization selective transmission of the chiral metasurface, a pair of enantiomers have been employed to achieve high-resolution nonlinear chiral high-contrast imaging, which further improves the information DOF of the multifunctional coding metasurface. Our scheme and design method paves the way for integrated informational metasurface that enables high-order information channels in both linear and nonlinear regimes and may find applications in chiral detection and information encryption.

4. Experimental Section

Sample Fabrication: The all-dielectric silicon metasurfaces were fabricated on a fused silica wafer with deposition, standard EBL lift-off, and etching procedure. First, a 480 nm-thick hydrogenated amorphous silicon (a-Si:H) film was deposited onto the substrate by plasma-enhanced chemical vapor deposition (PECVD). A thin ZEP520A resist layer with a thickness of 300 nm was spin-coated onto the a-Si:H film and baked on a hot plate at 170 °C for 2 min, then e-spacer (a 300Z, Showa Electrician) was subsequently coated to prevent the electron beam from charging during exposure. As a next step, the meta-atoms were patterned by using standard electron beam lithography (Raith150) which employing a 30 kV voltage, 20 pA current, and 150 μC cm^{-2} dose, followed by developed *n*-amyl acetate for 60 s. A 60 nm-thick aluminum film was
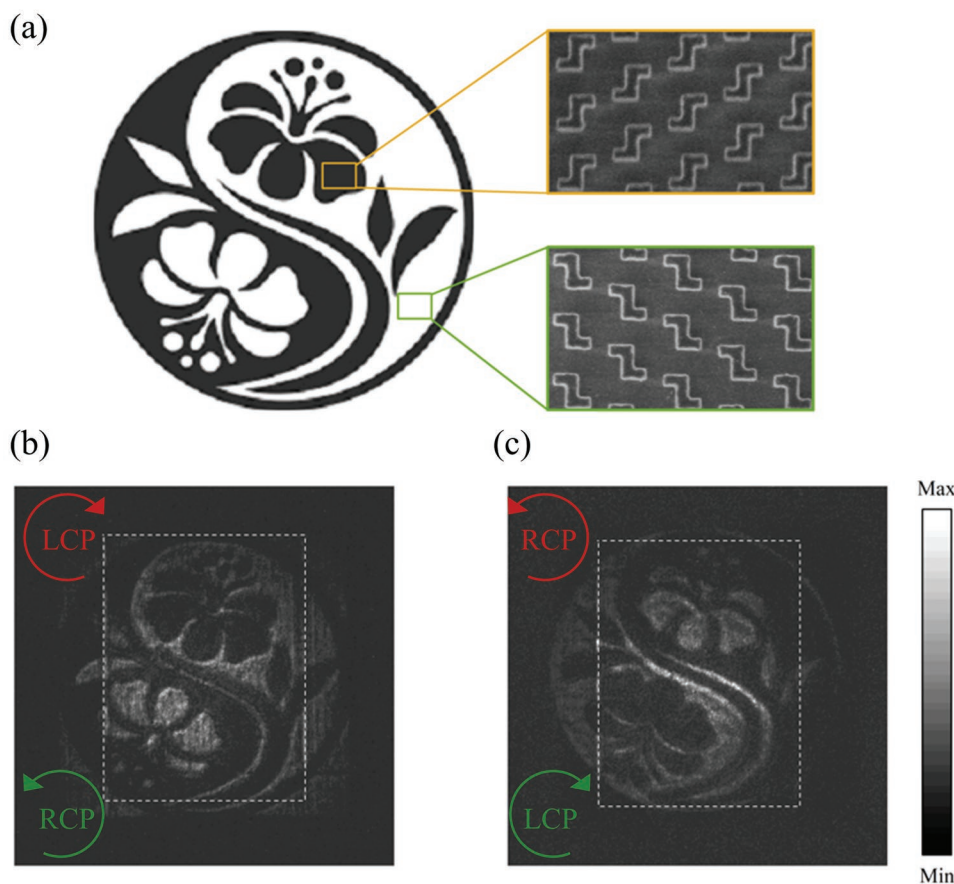

Figure 6. Measured nonlinear chiral high-contrast imaging. a) Schematic of the designed flower pattern. The black and white regions of the pattern are formed by the resonators (yellow box) and the enantiomers (green box), respectively. b,c) Captured nonlinear images of the flower pattern under (b) LCP and (c) RCP incidence with cross-polarization detection.

deposited on the substrate by electron beam evaporation (Temescal BJD-2000) and patterned using a solvent (ZDMAC, Zeon Co.) to lift off the resist. The patterned aluminum was used as a hard mask during dry etching to transfer the designed pattern onto the underlying a-Si:H layer by fluorine-based inductively coupled plasma reactive ion etching (Oxford Plasmalab System 100). The process parameters of the ICP-RIE were 20 sccm of CHF3 + 3 sccm of SF6 at 15 mTorr. The bias power was 20 W and the induction power was 500 W. The aluminum remaining on the patterned nanoparticles was removed by wet etching. Finally, a SU-8 polymer layer with a thickness of 500 nm was spin-coated onto the structures and UV-cured. The total size of the metasurface was 200 μm.

Simulation Methods: To find specific structure geometries that introduce high nonlinear conversion efficiency at the excitation wavelength of 1550 nm (the center wavelength of femtosecond laser), full-wave nonlinear simulations of amorphous silicon particles on glass substrate using the finite element method solver of COMSOL multiphysics were performed. It has two steps to calculate the radiated nonlinear emission based on an undepleted pump approximation. First, the linear scattering at the fundamental wavelength of 1550 nm was calculated. Next step, THG electromagnetic simulation was studied with the nonlinear polarization introduced by the fundamental resonance. The nonlinear susceptibility tensor $\chi^{(3)}$ was considered as a constant scalar value of 2.45×10^{-19}. All calculations were realized for a single amorphous silicon Z resonator placed on a semi-infinite glass substrate with periodic boundary conditions at opposite side directions to imitate an orthohexagnal array with a 595 nm period. The sub-wavelength scale periodicity was set to avoid high-order diffraction. Circularly polarized lights were vertically illuminated on the chiral metasurface from the substrate side and perfectly matched layers were employed along the z-direction.

Measurement Procedure: An erbium-doped ultrafast fiber laser (Toptica Photonics AG FemtoFiber Pro NIR, repetition frequency: 80 MHz, pulse length: ≈80 fs) centered at 1550 nm was applied as the fundamental beam source. Followed by an LP and a QWP to create circular polarization. Then the light was normally illuminated on the metasurface from the substrate side. Generated linear and nonlinear signals were analyzed by another set of QWP and LP to make sure the specific circular polarization light was collected with the objective, tube lens (Thorlabs ITL200), and scientific camera that was integrated on an XYZ-axis motorized translation stage to scan the focusing profiles and the multichannel optical vortices with a step of 0.5 μm along the transmitted direction. For fundamental measurement, the excitation beam average power was set to 1 mW, and the transmitted signal was collected with a 50× objective (SIGMA-KOKI PAL-50-NIR-HR-LC00 50× NA = 0.67) and an InGaAs camera (HAMAMATSU InGaAs C10633), the lens and short-pass filters were removed. For nonlinear measurement, the fundamental pulse with an average power of 350 mW was focused on the sample with a diameter of ≈200 μm after a lens with a focal length of 150 mm. Followed by filters the THG signals were captured by a 20× objective (SIGMA-KOKI PAL-20-NIR-HR-LC00 20× NA = 0.45) and an sCMOS camera (HAMAMATSU ORCA-Flash4.0 V3) without fundamental interference.

Conflict of Interest

The authors declare no conflict of interest.

Data Availability Statement

The data that support the findings of this study are available from the corresponding author upon reasonable request.

[1] S. Mokashi-punekar, Y. Zhou, S. C. Brooks, N. L. Rosi, *Adv. Mater.* **2020**, *32*, 1905975.

[2] J. García-Guirado, M. Svedendahl, J. Puigdollers, R. Quidant, *Nano Lett.* **2020**, *20*, 585.

[3] A. Basiri, X. Chen, J. Bai, P. Amrollahi, J. Carpenter, Z. Holman, C. Wang, Y. Yao, *Light: Sci. Appl.* **2019**, *8*, 78.

[4] A. B. Khanikaev, N. Arju, Z. Fan, D. Purtseladze, F. Lu, J. Lee, P. Sarriugarte, M. Schnell, R. Hillenbrand, M. A. Belkin, G. Shvets, *Nat. Commun.* **2016**, *7*, 12045.

[5] E. W. Wang, T. Phan, S. Yu, S. Dhuey, J. A. Fan, *Proc. Natl. Acad. Sci. USA* **2022**, *119*, e2122085119.

[6] J. Mun, M. Kim, Y. Yang, T. Badloe, J. Ni, Y. Chen, C. W. Qiu, J. Rho, *Light: Sci. Appl.* **2020**, *9*, 139.

[7] V. E. Bochenkov, T. I. Shabatina, *Biosensors* **2018**, *8*, 120.

[8] M. V. Gorkunov, A. A. Antonov, Y. S. Kivshar, *Phys. Rev. Lett.* **2020**, *125*, 093903.

[9] Y. Chen, X. Yang, J. Gao, *Light: Sci. Appl.* **2019**, *8*, 45.

[10] Y. Chen, W. Chen, X. Kong, D. Wu, J. Chu, C. W. Qiu, *Phys. Rev. Lett.* **2022**, *128*, 146102.

[11] S. D. Assimonis, V. Fusco, *Sci. Rep.* **2019**, *9*, 12334.

[12] Q. He, S. Sun, S. Xiao, L. Zhou, *Adv. Opt. Mater.* **2018**, *6*, 1800415.

[13] N. Yu, F. Capasso, *Nat. Mater.* **2014**, *13*, 139.

[14] Z. Li, R. Pestourie, J. S. Park, Y. W. Huang, S. G. Johnson, F. Capasso, *Nat. Commun.* **2022**, *13*, 2409.

[15] J. Cai, F. Zhang, M. Pu, Y. Chen, Y. Guo, T. Xie, X. Feng, X. Ma, X. Li, H. Yu, X. Luo, *Nanophotonics* **2022**, *11*, 1961.

[16] V. Ginis, M. Piccardo, M. Tamagnone, J. Lu, M. Qiu, S. Kheifets, F. Capasso, *Science* **2020**, *369*, 436.

[17] S. Chen, Z. Li, W. Liu, H. Cheng, J. Tian, *Adv. Mater.* **2019**, *31*, 1802458.

[18] B. Yang, W. Liu, Z. Li, H. Cheng, D. Y. Choi, S. Chen, J. Tian, *Nano Lett.* **2019**, *19*, 4221.

[19] J. S. T. Smalley, X. Ren, J. Y. Lee, W. Ko, W. J. Joo, H. Park, S. Yang, Y. Wang, C. S. Lee, H. Choo, S. Hwang, X. Zhang, *Nat. Commun.* **2020**, *11*, 3916.

[20] M. F. Limonov, M. V. Rybin, A. N. Poddubny, Y. S. Kivshar, *Nat. Photonics* **2017**, *11*, 543.

[21] A. Overvig, N. Yu, A. Alù, *Phys. Rev. Lett.* **2021**, *126*, 073001.

[22] T. Yoda, M. Notomi, *Phys. Rev. Lett.* **2020**, *125*, 053902.

[23] L. Raju, K. T. Lee, Z. Liu, D. Zhu, M. Zhu, E. Poutrina, A. Urbas, W. Cai, *ACS Nano* **2022**, *16*, 3926.

[24] Z. Hu, D. Bongiovanni, D. Jukić, E. Jajtić, S. Xia, D. Song, J. Xu, R. Morandotti, H. Buljan, Z. Chen, *Light: Sci. Appl.* **2021**, *10*, 164.

[25] Z. Hao, W. Liu, Z. Li, Z. Li, G. Geng, Y. Wang, H. Cheng, H. Ahmed, X. Chen, J. Li, J. Tian, S. Chen, *Laser & Photonics Rev.* **2021**, *15*, 2100207.

[26] S. Liu, P. P. Vabishchevich, A. Vaskin, J. L. Reno, G. A. Keeler, M. B. Sinclair, I. Staude, I. Brener, *Nat. Commun.* **2018**, *9*, 2507.

**ADVANCED
SCIENCE NEWS**

www.advancedsciencenews.com

**ADVANCED
OPTICAL
MATERIALS**

www.advopticalmat.de

[27] D. D. Hickstein, F. J. Dollar, P. Grychtol, J. L. Ellis, R. Knut, C. Hernandez-Garcia, D. Zusin, C. Gentry, J. M. Shaw, T. Fan, K. M. Dorney, A. Becker, A. Jaron-Becker, H. C. Kapteyn, M. M. Murnane, C. G. Durfee, *Nat. Photonics* **2015**, *9*, 743.

[28] H. Liu, C. Guo, G. Vampa, J. L. Zhang, T. Sarmiento, M. Xiao, P. H. Bucksbaum, J. Vučković, S. Fan, D. A. Reis, *Nat. Phys.* **2018**, *14*, 1006.

[29] E. Maguid, I. Yulevich, D. Veksler, V. Kleiner, M. L. Brongersma, E. Hasman, *Science* **2016**, *352*, 1202.

[30] J. Y. Dai, J. Zhao, Q. Cheng, T. J. Cui, *Light: Sci. Appl.* **2018**, *7*, 90.

[31] P. Zheng, Q. Dai, Z. Li, Z. Ye, J. Xiong, H. C. Liu, G. Zheng, S. Zhang, *Sci. Adv.* **2021**, *7*, eabg0363.

[32] Z. Li, W. Liu, G. Geng, Z. Li, J. Li, H. Cheng, S. Chen, J. Tian, *Adv. Funct. Mater.* **2020**, *30*, 1910744.

[33] M. Ma, Z. Li, W. Liu, C. Tang, Z. Li, H. Cheng, J. Li, S. Chen, J. Tian, *Laser Photonics Rev.* **2019**, *13*, 1900045.

[34] A. C. Overvig, S. C. Malek, N. Yu, *Phys. Rev. Lett.* **2020**, *125*, 017402.

[35] H. Wu, X. X. Gao, L. Zhang, G. D. Bai, Q. Cheng, L. Li, T. J. Cui, *Light: Sci. Appl.* **2020**, *9*, 198.

[36] T. J. Cui, L. Li, S. Liu, Q. Ma, L. Zhang, X. Wan, W. X. Jiang, Q. Cheng, *iScience* **2020**, *23*, 101403.

[37] G. Li, S. Chen, N. Pholchai, B. Reineke, P. W. H. Wong, E. Y. B. Pun, K. W. Cheah, T. Zentgraf, S. Zhang, *Nat. Mater.* **2015**, *14*, 607.

[38] C. Menzel, C. Rockstuhl, F. Lederer, *Phys. Rev. A* **2010**, *82*, 053811.

[39] S. Zanotto, G. Mazzamuto, F. Riboli, G. Biasiol, G. C. L. Rocca, A. Tredicucci, A. Pitanti, *Nanophotonics* **2019**, *8*, 2291.

[40] M. Khorasaninejad, K. B. Crozier, *Nat. Commun.* **2014**, *5*, 5386.

[41] S. Keren-Zur, O. Avayu, L. Michaeli, T. Ellenbogen, *ACS Photonics* **2016**, *3*, 117.

[42] C. Schlickriede, S. S. Kruk, S. S. Kruk, L. Wang, B. Sain, Y. Kivshar, T. Zentgraf, *Nano Lett.* **2020**, *20*, 4370.

[43] W. Zhao, K. Wang, X. Hong, B. Wang, X. Han, H. Long, B. Wang, P. Lu, *Nanoscale* **2020**, *12*, 13330.

[44] P. Huo, C. Zhang, W. Zhu, M. Liu, S. Zhang, S. Zhang, L. Chen, H. J. Lezec, A. Agrawal, Y. Lu, T. Xu, *Nano Lett.* **2020**, *20*, 2791.